Science Current Issue First release papers Archive About Submit man

HOME > SCIENCE > VOL. 386, NO. 6723 > HIGH-TEMPERATURE CARBON DIOXIDE CAPTURE IN A POROUS MATERIAL WITH TERMINAL ZINC HYDRIDE SITES

RESEARCH ARTICLE | GREENHOUSE GASES

# High-temperature carbon dioxide capture in a porous material with terminal zinc hydride sites

RACHEL C. ROHDE, KURTIS M. CARSCH, MATTHEW N. DODS, HENRY Z. H. JIANG, ALEXANDRA R. MCISAAC, RYAN A. KLEIN, HYUNCHUL KWON, SARAH L. KARSTENS, YANG WANG, [...], AND JEFFREY R. LONG +13 authors Authors Info & Affiliations

SCIENCE • 14 Nov 2024 • Vol 386, Issue 6723 • pp. 814-819 • DOI: 10.1126/science.adk5697

Institute for Decarbonization Materials, University of California, Berkeley, CA 94720, USA.

Department of Chemistry, University of California, Berkeley, CA 94720, USA.

Department of Chemical and Biomolecular Engineering, University of California, Berkeley, CA 94720, USA.

Materials Sciences Division, Lawrence Berkeley National Laboratory, Berkeley, CA 94720, USA.

Department of Materials Science and Engineering, University of California, Berkeley, CA 94720, USA.

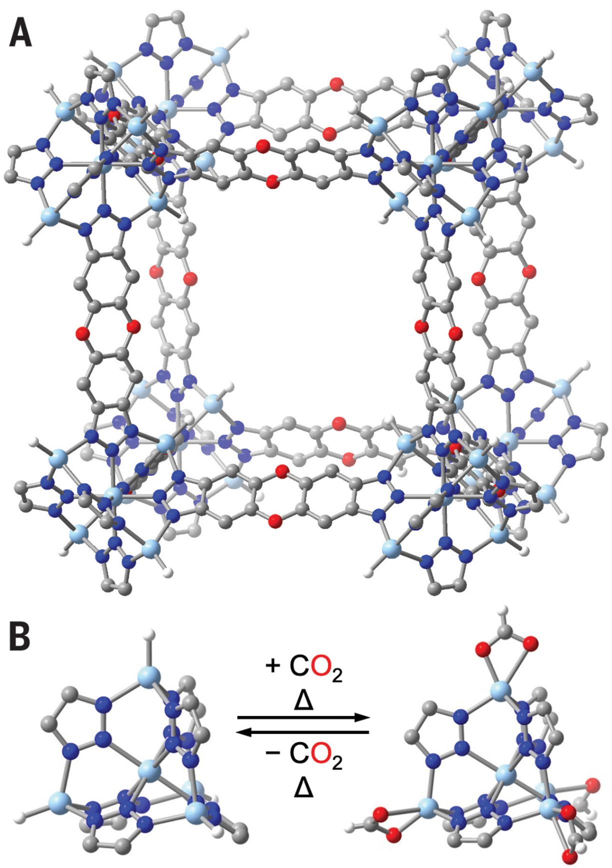


Published on 14 Nov, 2024

Sonali
15.03.2025

# Background

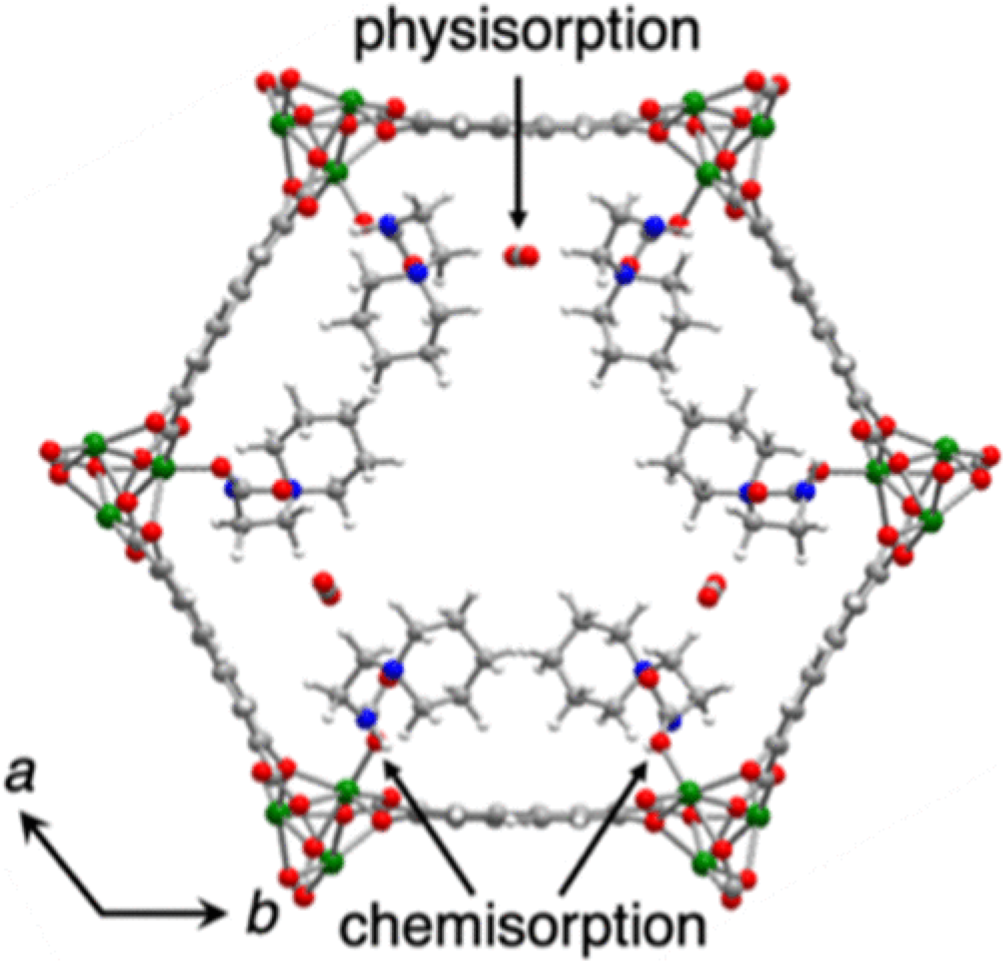


- Amine-based MOFs have been used for $CO_2$ capture.
- Drawbacks with these MOFs are high heat capacities, volatility, and corrosivity of amines, which limit their usage.
- It is still difficult to capture $CO_2$ at high temperatures above 150 ºC.

## Why this paper?

- Zinc-hydride sites reversibly bind $CO_2$ at temperatures above 200 °C.
- Excellent stability at high temperatures.

## Column breakthrough experiment

The column is packed with pelletized Zn-H MOF and exposed to 20% or 4% $CO_2$ gas at 280 ºC to simulate realistic conditions.

Data was collected until no $CO_2$ was detected in the outlet.

# Introduction

Ligand used for MOF

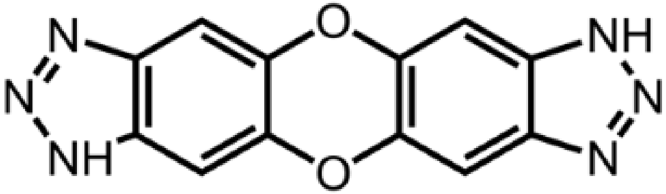


L1

**3.2. Synthesis of $Zn_5Br_4(btdd)_3$ (ZnBr-MFU-4*l*).**

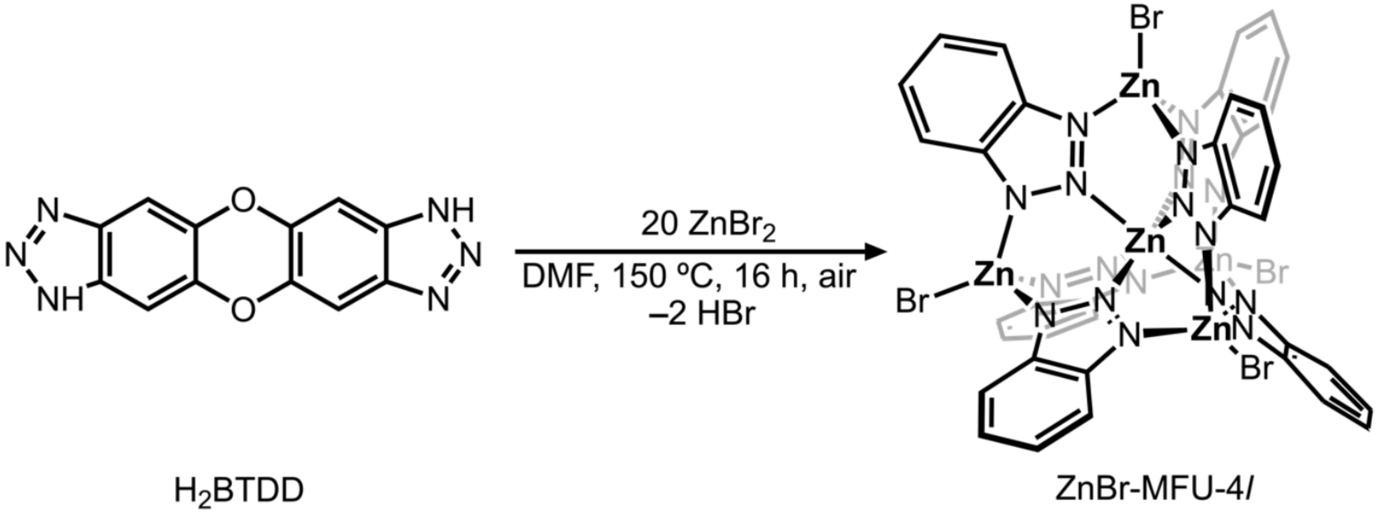

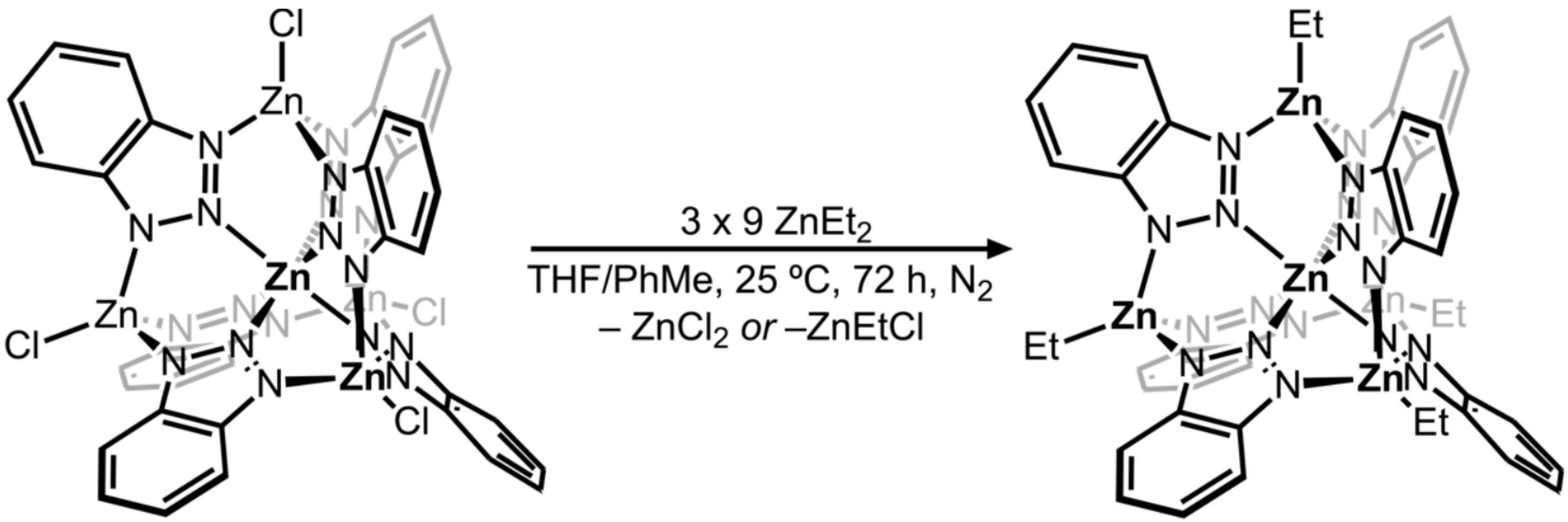


ZnCl-MFU-4*l* ZnEt-MFU-4*l*

**3.6. Synthesis of Zn($O_2$CH)-MFU-4*l* ($Zn_5(O_2CH)_{3.76}Cl_{0.24}(btdd)_3$).**

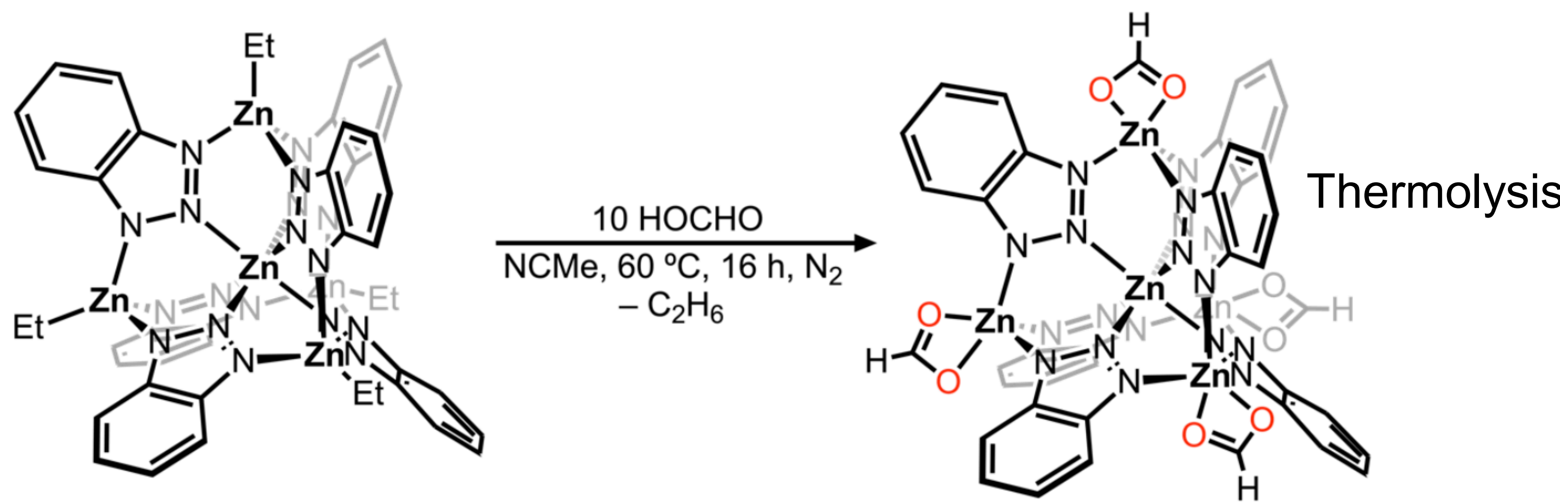


ZnEt-MFU-4*l* Zn(OCHO)-MFU-4*l*

(A)

# Powder neutron diffraction data

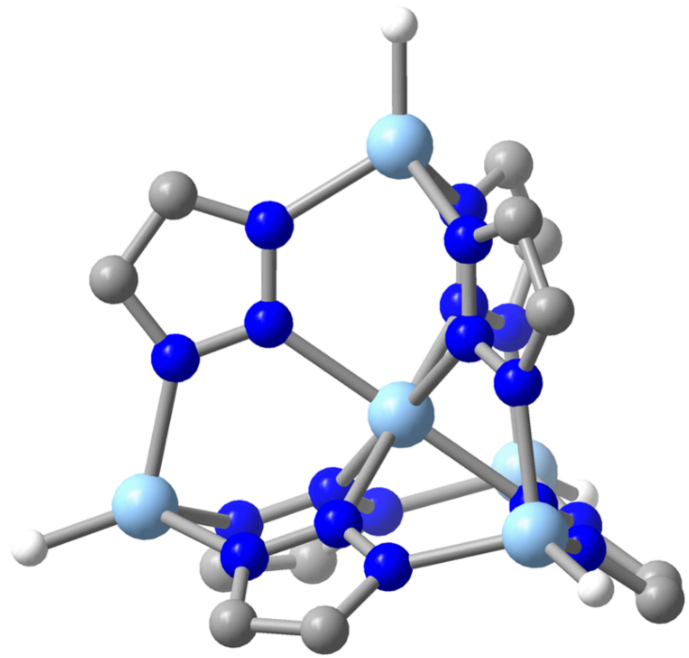

**Figure S97.** Portion of the solid-state structure of ZnH-MFU-4*l* solved from powder neutron diffraction showing a pentanuclear node as a ball-and-stick model. Light blue, dark blue, and gray spheres represent Zn, N, and C atoms respectively. CCDC entry value: 2352001.

**Table S23.** Selected bond parameters for ZnH-MFU-4*l*.

| | | | |
|---|---|---|---|
| Zn2–N1 | 2.072(12) Å | Zn2–H1 | 1.56(2) Å |
| Zn1–N2 | 2.190(8) Å | ∠Zn1–Zn2–H1 | 180.0(0) ° |
| Zn1–Zn2 | 3.660(7) Å | ∠N2–Zn2–H1 | 121.5(5) ° |

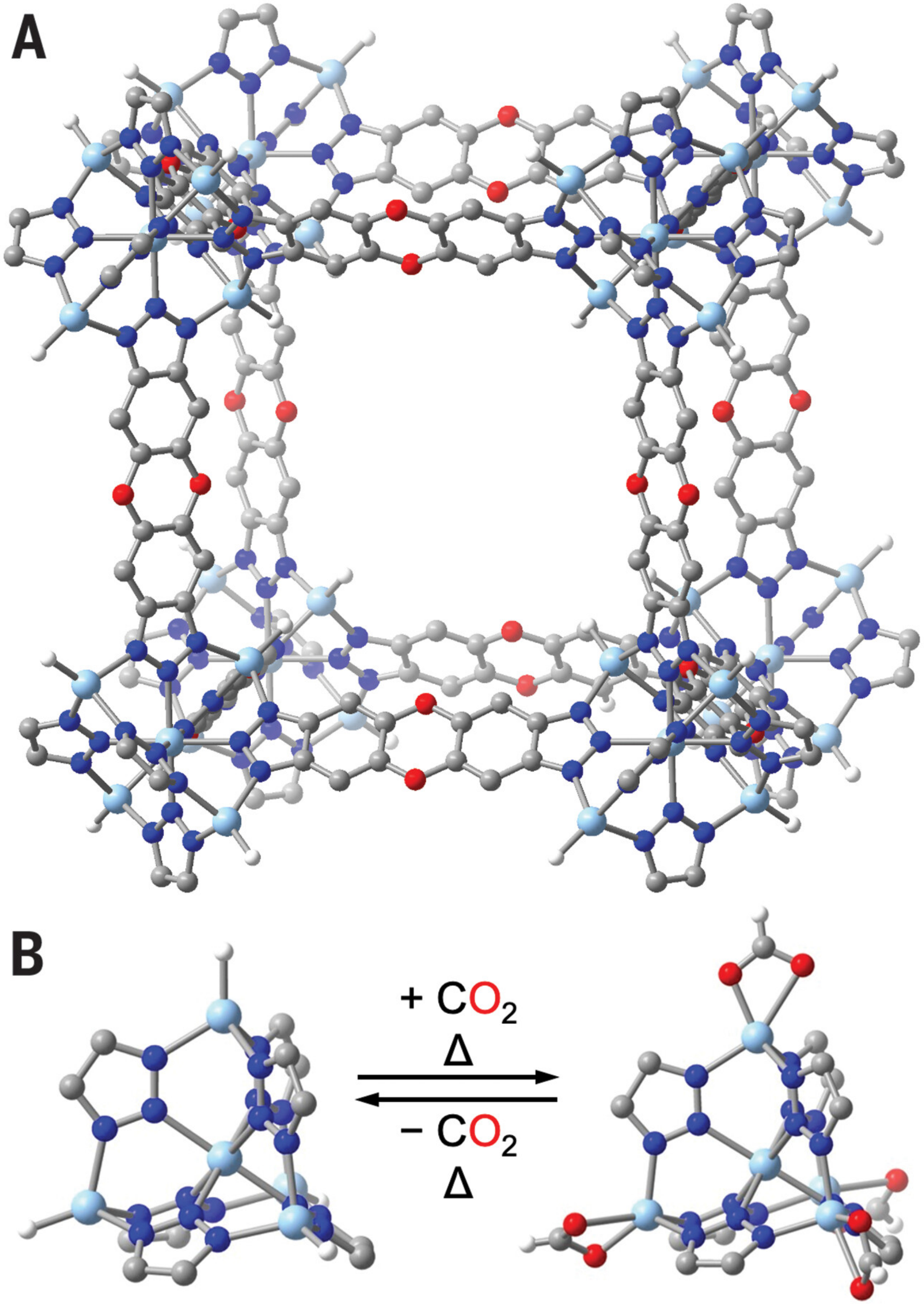


**Fig. 1. Reversible high-temperature $CO_2$ capture in a zinc hydride MOF.** (**A**) A portion of the structure of ZnH-MFU-4*l*, as determined from single-crystal x-ray diffraction analysis. (**B**) (Left) Expanded view of a pentanuclear cluster node of the framework [$d_{Zn–H}$= 1.546(9) Å, N–Zn–H = 121.2(4)°; table S20]. (Right) At temperatures above 200°C, $CO_2$ reversibly inserts into the Zn–H bonds of ZnH-MFU-4*l* to generate Zn–formate species [$d_{Zn–O}$ = 1.971(6) and 2.408(4) Å, O–C–O = 119.2(6)°; table S21]. Light-blue, gray, blue, red, and white spheres represent Zn, C, N, O, and H atoms, respectively.

## Stability of the MOF

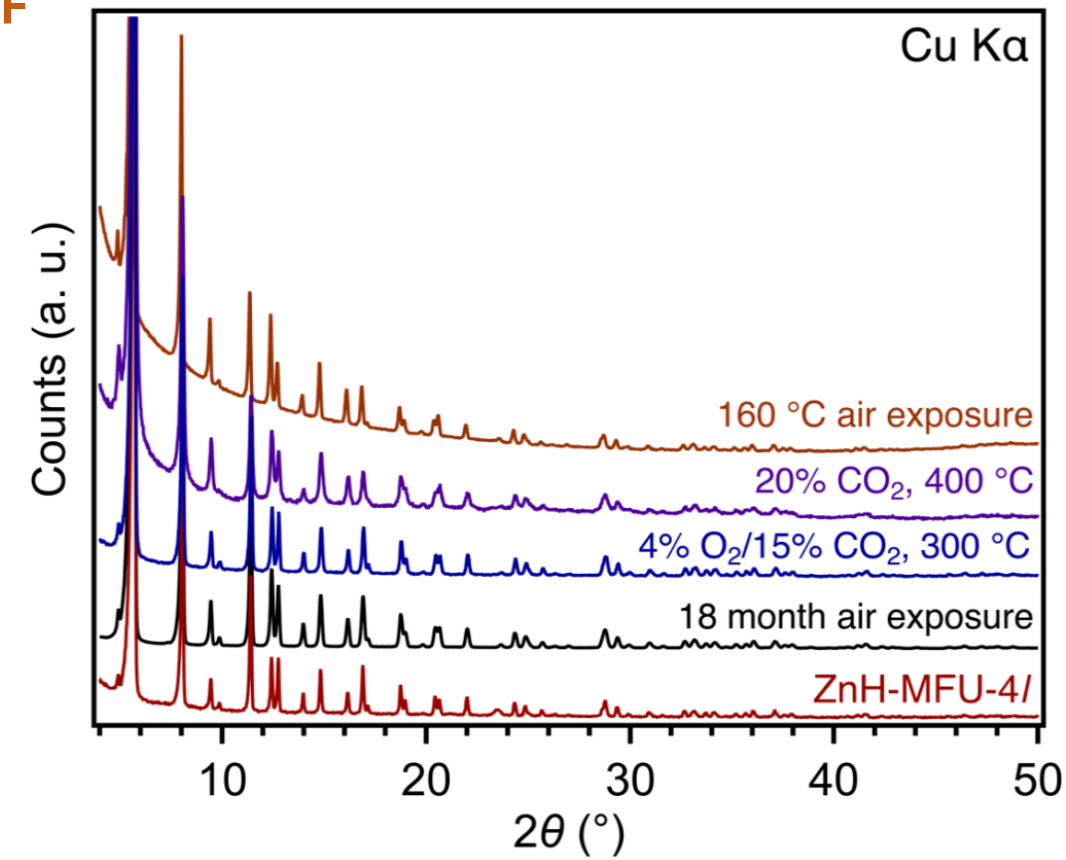


**Figure S82.** Comparison of powder x-ray diffraction patterns (Cu Kα radiation) collected under air for (bottom to top): pristine ZnH-MFU-4*l*, ZnH-MFU-4*l* after 18-month exposure to air at ambient temperature; ZnH-MFU-4*l* following $CO_2$ adsorption–desorption cycling in the presence of $O_2$ (adsorption: 4% $O_2$, 15% $CO_2$, 81% $N_2$; desorption under 100% $N_2$; see Figure S35) at 300 °C; ZnH-MFU-4*l* following adsorption–desorption cycling in the presence of only $CO_2$ and $N_2$ (adsorption: 20% $CO_2$/80%; desorption: pure $N_2$ at 400 °C; see Figure S33); and ZnH-MFU-4*l* following exposure to 160 °C air for 12 h. Similar reflections in all patterns indicate the retention of long-range framework crystalline order, indicative of stability under these diverse conditions. Note that the asymmetry in the 18-month exposure pattern is not due to $CO_2$ insertion, but likely due to the presence of residual chlorides bound to the Zn site. Indeed, IR spectroscopy analysis of the same sample and $^1$H NMR spectroscopy analysis of an acid digested portion of the sample did not reveal any formate anion.

# $CO_2$ Adsorptions at different temp

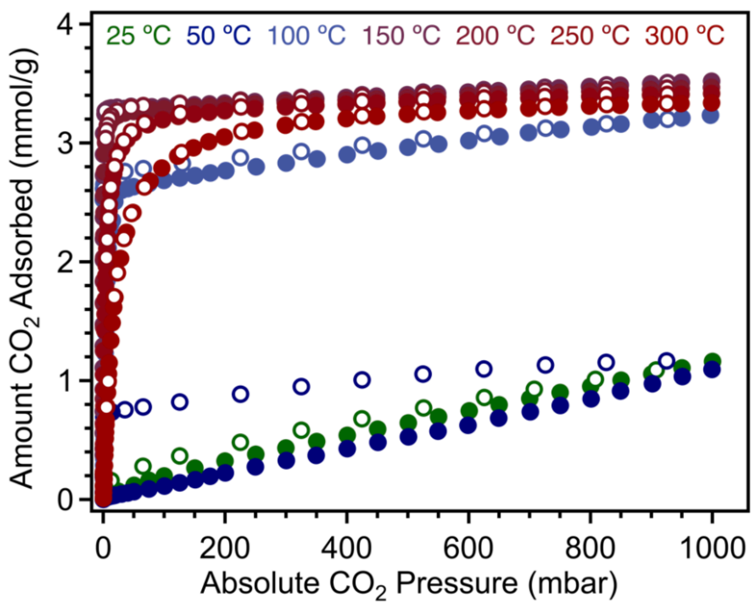


Comparison of $CO_2$ adsorption (filled circles) and desorption (open circles) isotherms for ZnH-MFU-4*l* at 25, 50, 100, 150, 200, 250, and 300 °C. (Lower)

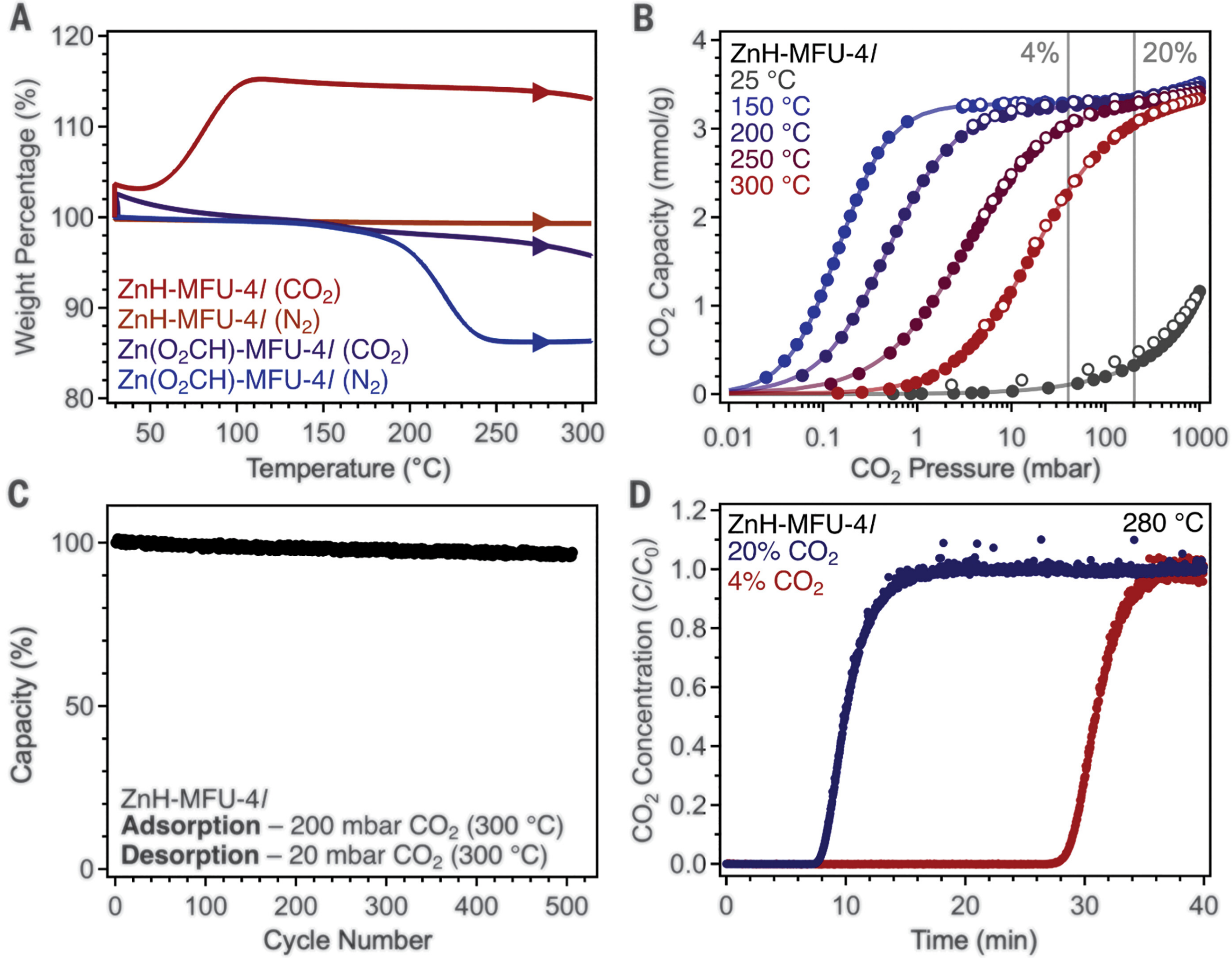


**Fig. 2. High-temperature isobaric and isothermal $CO_2$ adsorption data for ZnH-MFU-4*l*.**
(**A**) Thermogravimetric analysis data collected for ZnH-MFU-4*l* or Zn($O_2$CH)-MFU-4*l* under an atmosphere of pure $CO_2$ or $N_2$. (**B**) Variable-temperature $CO_2$ adsorption (filled circles) and desorption (open circles) isotherms for ZnH-MFU-4*l*. Solid lines are guides for the eyes. Vertical lines denote $CO_2$ concentrations relevant to flue streams produced from natural gas combine cycles and single-cycle turbines (~4% $CO_2$) and cement and steelmaking (20% $CO_2$ and higher) (*18*, *32*, *33*). (**C**) Cycling data for ZnH-MFU-4*l* during the course of 508 isothermal adsorption (200 mbar $CO_2$) and desorption under vacuum (20 mbar $CO_2$) cycles at 300°C, plotted as a percentage of the capacity measured for the first cycle (1.24 mmol/g). Note that the chosen desorption pressure would achieve only partial $CO_2$ desorption, and the measured capacities are consistent with those expected with this desorption pressure, as indicated by the isothermal data. The capacity in the final cycle was 1.19 mmol/g. See section 2.4 of the SM for experimental details and fig. S27 for the raw data. (**D**) Breakthrough data collected for a pelletized sample of ZnH-MFU-4*l* exposed to a flowing (10 sccm) gas stream at ~280°C consisting of 20% $CO_2$ in $N_2$ (blue data) or 4% $CO_2$ in $N_2$ (red data). See sections 2.8 and 7 of the SM for experimental details.

### 4.4. Isosteric enthalpies of adsorption.

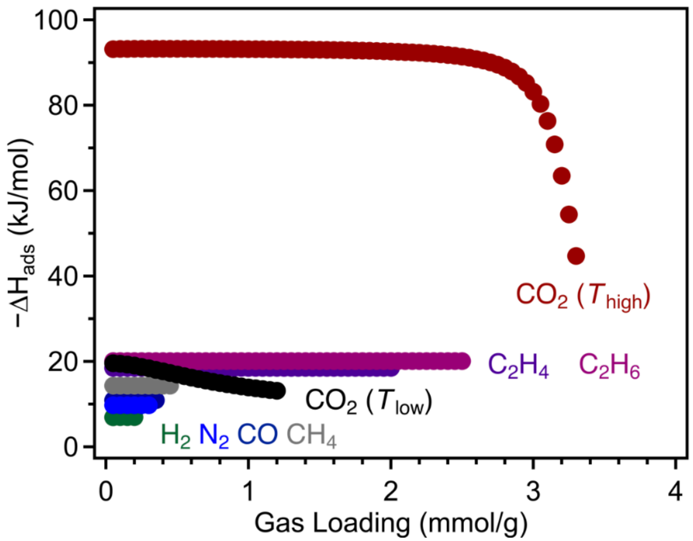


**Figure S24.** Calculated isosteric enthalpies of adsorption ($\Delta H_{ads}$) for various gases in ZnH-MFU-4*l* as a function of loading, determined using the Clausius–Clapeyron equation (see Section 2.6 for details). Note these data were obtained based on fits to adsorption isotherms collected over different temperature ranges for each gas (see Table S5).

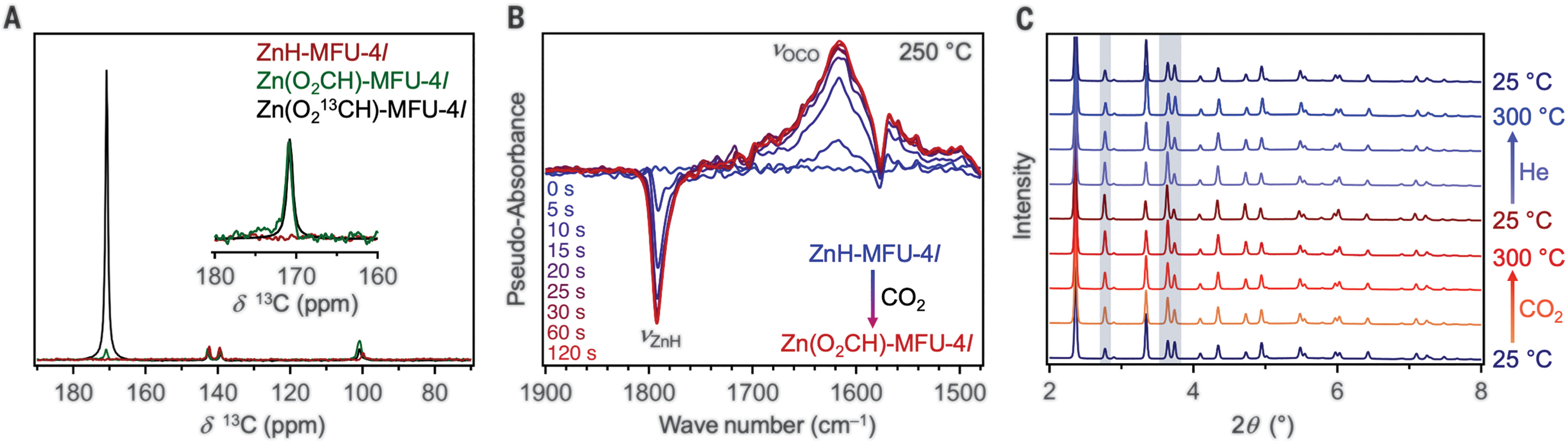


**Fig. 3. Spectroscopic and structural characterization of reversible $CO_2$ uptake in ZnH-MFU-4*l*.** (**A**) Solid-state $^{13}C\{^1H\}$ cross polarization NMR spectra (magic angle spin rates of 20 kHz) for ZnH-MFU-4*l*, $Zn(O_2CH)$-MFU-4*l*, and ZnH-MFU-4*l* dosed with 1 bar $^{13}CO_2$ at ~280°C, revealing a peak at 170.8 ppm corresponding to formate in $Zn(O_2CH)$-MFU-4*l* and $Zn(O_2{}^{13}CH)$-MFU-4*l*. The inset depicts the intensity-normalized formate $^{13}C$ resonance. (**B**) Difference spectra obtained from subtracting time-resolved DRIFTS data for a sample of ZnH-MFU-4*l* dosed in situ with 200 mbar $CO_2$ at 250°C from a spectrum collected for ZnH-MFU-4*l* at 250°C (*t* = 0 corresponds a spectrum collected immediately before dosing). (**C**) Representative powder x-ray diffraction patterns collected during the course of the in situ gas-dosing experiment. Starting from a sample of ZnH-MFU-4*l* cooled from 300° to 25°C under He (bottom blue trace), diffraction patterns (λ = 0.45207 Å) were collected for ZnH-MFU-4*l* during the course of heating from 25° to 300°C and then cooling under flowing $CO_2$(10 sccm, orange to dark-red traces); heating from 25° to 300°C under He to desorb $CO_2$; and finally cooling to 25°C under He (10 sccm; blue traces). Rietveld refinements of the top and bottom patterns indicate that the structure of ZnH-MFU-4*l*is the same after cycling. Select patterns are shown to highlight changes with heating under the different gas atmospheres. Highlighted reflections are diagnostic of structural changes. Additional diffraction patterns are provided in fig. S86

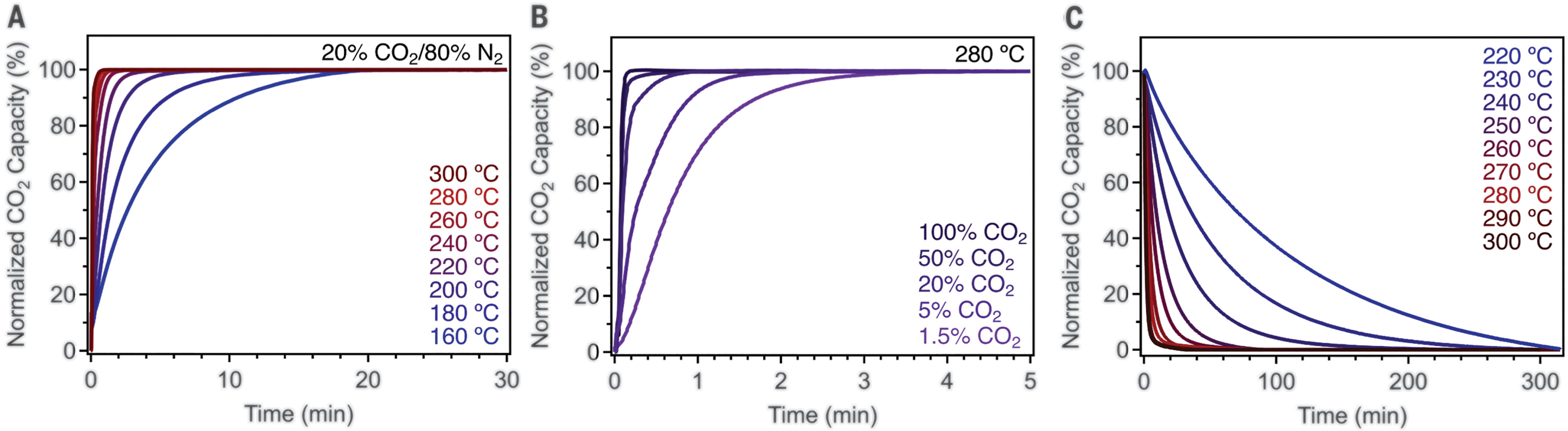


**Fig. 4. Kinetics of $CO_2$ adsorption and desorption.**
(**A**) Kinetic adsorption profiles collected for ZnH-MFU-4*l* exposed to a flowing 20% $CO_2$ stream with $N_2$ balance at ~1 bar and temperatures ranging from 160° to 300°C (see section 2.13.2 of the SM for details). Saturation with $CO_2$ occurred more rapidly as the temperature of the gas stream was increased. (**B**) Kinetic adsorption profiles collected for ZnH-MFU-4*l* at 280°C exposed to flowing gas streams (~1 bar) with $CO_2$ concentrations ranging from 1.5% $CO_2$ (balance $N_2$) to 100% $CO_2$. Saturation with $CO_2$ occurred more rapidly as the concentration of $CO_2$ was increased. (**C**) Variable-temperature kinetic desorption profiles collected for Zn($O_2$CH)-MFU-4*l* under flowing $N_2$ (see section 2.13.4 of the SM for details). All measurements were conducted under a flow rate of 100 sccm with a thermogravimetric analyser

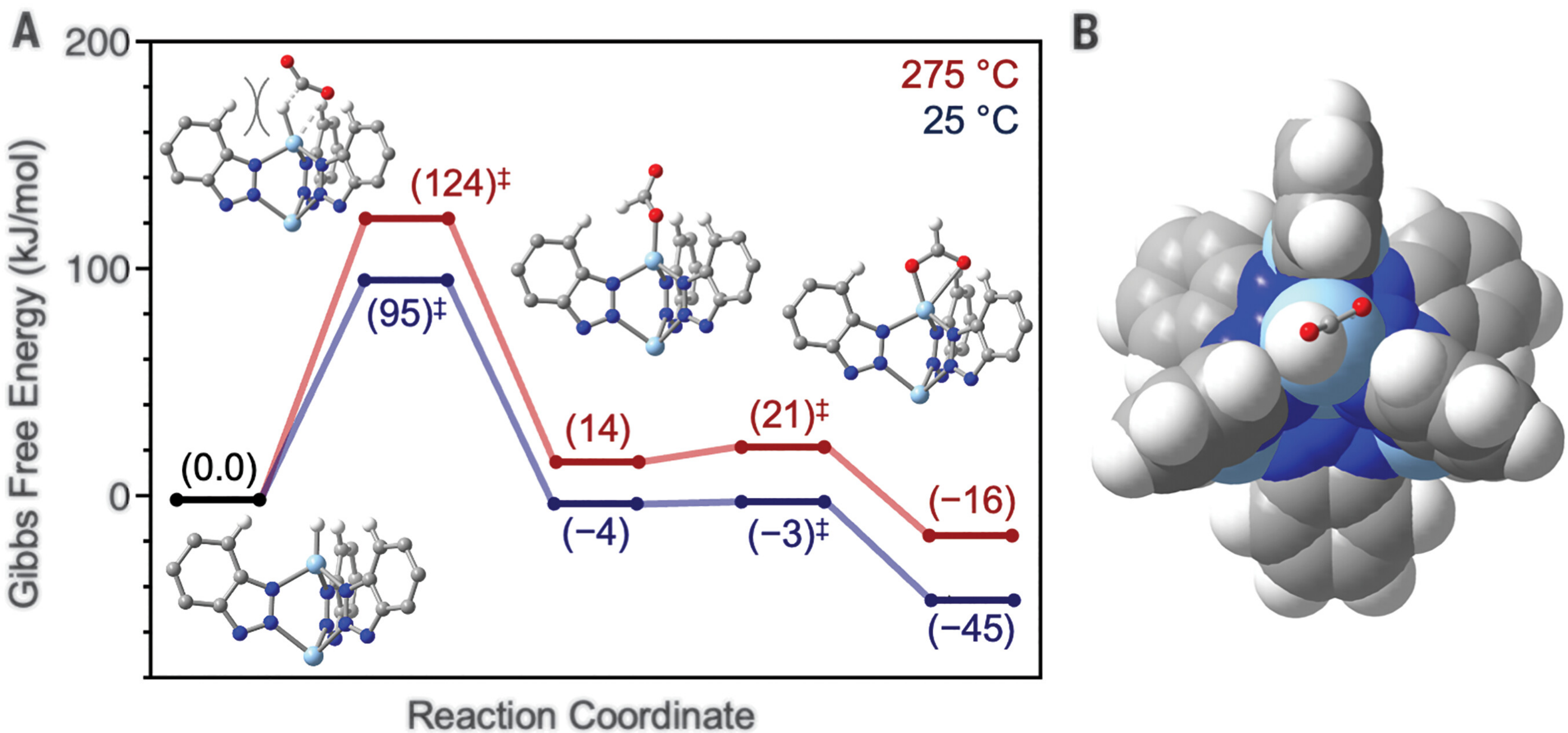


**Fig. 5. Calculated free-energy landscape for $CO_2$ insertion into the Zn–H bond.**
(**A**) Free-energy landscape for the reaction of $CO_2$with the model $Zn_5H_4(bta)_6$ cluster to yield $Zn_5(O_2CH)_4(bta)_6$ at 25° and 275°C. The large barrier to $CO_2$ insertion (95 kJ/mol at 25°C) is consistent with the absence of $CO_2$ insertion reactivity at ambient temperature. At 275°C, there is still a large barrier to $CO_2$ insertion, but adsorption remains thermodynamically favored (see table S25), and high temperature provides enough thermal energy to overcome this barrier (see section 12 of the SM for computational details). (**B**) An overhead view of space-filling models illustrating the calculated transition state for $CO_2$insertion into the Zn–H bond of $Zn_5H_4(bta)_6$. As the $CO_2$ approaches the metal center, the hydride ligand is displaced and comes into close contact with one of the $bta^-$ ligands (distance of 2.42 Å, or approximately two times the van der Waals radius of hydrogen) (47). This unfavorable interaction likely contributes to the large activation barrier for $CO_2$ insertion

# Conclusions

Zn-H MOF demonstrates the ability to reversibly bind $CO_2$ at temperatures above 200 °C.

Zn-H MOF captures effectively and rapidly from various point sources, including industrial exhausts and efficient even in low $CO_2$ conditions.